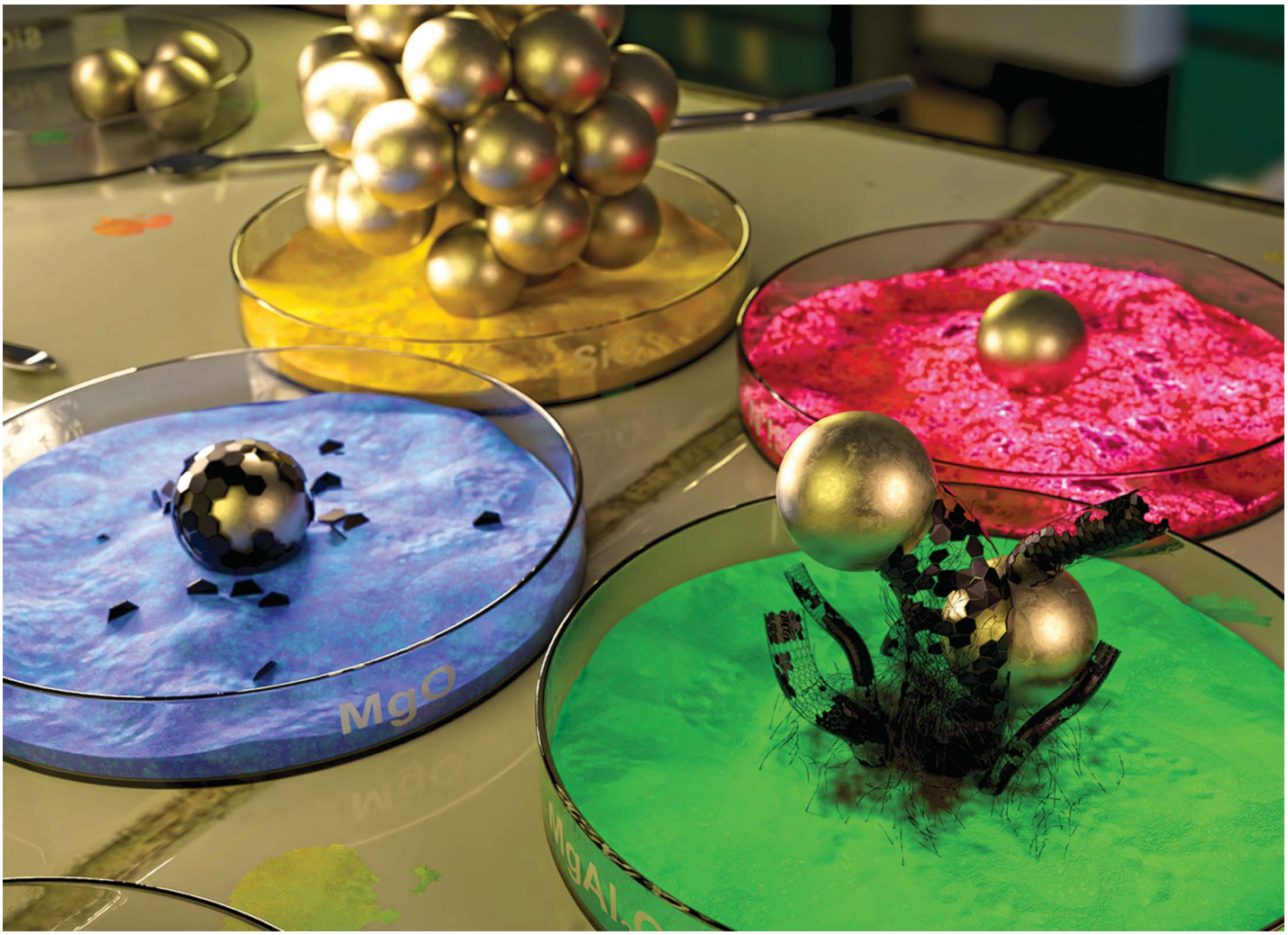

Showcasing research from Dr Esteban Gioria and Prof. Christian Damsgaard's laboratory, DTU Physics, Technical University of Denmark.

Colloidal Fe nanocrystals for CH_4 decomposition: role of the support

The nature of the support can drastically influence catalytic activity. In this work, carried out at the Department of Physics, Technical University of Denmark, E. Gioria and co-workers demonstrated how preformed Fe nanocrystals catalyse CH_4 decomposition into various carbon nanostructures. Among the supports tested, only $MgAl_2O_4$ enabled the formation of carbon nanotubes. MgO effectively anchored the Fe nanoparticles but encapsulating the Fe sites, SiO_2 led to significant sintering, and Si_3N_4 evidenced C_xN_y formation due to partial carburization of the support.

Image reproduced by permission of Esteban Gioria and Christian D. Damsgaard from *J. Mater. Chem. A*, 2025, **13**, 27136.

As featured in:

See Esteban Gioria, Christian D. Damsgaard *et al.*, *J. Mater. Chem. A*, 2025, **13**, 27136.

ROYAL SOCIETY OF CHEMISTRY

rsc.li/materials-a

Registered charity number: 207890

Journal of Materials Chemistry A

ROYAL SOCIETY OF CHEMISTRY

PAPER

View Article Online
View Journal | View Issue

Cite this: J. Mater. Chem. A, 2025, 13, 27136

Colloidal Fe nanocrystals for CH_4 decomposition: role of the support†

Esteban Gioria, *[a] Filippo Romeggio, [a] Ruben Bueno Villoro, [b] Ilenia Giarnieri, [c] Patricia Benito, [c] Ib Chorkendorff[a] and Christian D. Damsgaard *[abd]

Metal-supported nanoparticles play a crucial role in heterogeneous catalysis, with their activity governed by size, composition, and metal–support interactions. Conventional preparation methods often lack precise control of nanoparticle descriptors or introduce secondary metallic phases, limiting insights into intrinsic catalytic properties. In this study, colloidal iron nanoparticles (FeNPs) were used as pre-formed active sites to investigate CH_4 decomposition, a reaction that yields high-purity H_2 and carbon nanotubes (CNTs). FeNPs were supported on SiO_2, MgO, Si_3N_4 and $MgAl_2O_4$, to systematically assess the influence of support materials on catalytic activity and the nature and morphology of carbon products. Characterization *via ex situ* TEM, STEM-EDS, SEM, XPS, Raman spectroscopy, and *in situ* XRD revealed distinct support-dependent behaviors. Fe/SiO_2 exhibited deactivation due to severe sintering and encapsulation. Nevertheless, Fe_3C species were identified as a stable phase under reaction conditions. Fe/MgO showed high stability against sintering but severe FeNPs encapsulation. Surprisingly, FeNPs on Si_3N_4 retained their nanometric size, probably due to strong anchoring in the support. Nevertheless, the support partially reacts with CH_4 leading to C_3N_3 species. In contrast, Fe/$MgAl_2O_4$ demonstrated the highest activity towards carbon nanostructures formation, producing abundant CNTs *via* the tip growth and base growth mechanisms. Beam-enhanced *in situ* TEM confirmed a base growth process, with FeNPs remaining attached to the spinel support. The results evidenced the oxophylic nature of the support as an important descriptor of the stability of preformed FeNPs. This study provides a systematic comparison of colloidal FeNPs on various supports for CH_4 decomposition to form CNTs and CO_2-free H_2, offering insights into active phase formation, CNTs growth mechanisms, and optimal support selection for efficient CNTs production.

Received 8th May 2025
Accepted 2nd July 2025

DOI: 10.1039/d5ta03667d

rsc.li/materials-a

1 Introduction

Metal-supported nanoparticles are widely employed as heterogeneous catalysts in various chemical reactions. Their catalytic activity and selectivity toward desired products are strongly influenced by properties such as size, shape, and composition.[1] Additionally, the interaction between metal sites and the support plays a crucial role in determining catalytic performance. Key effects include hydrogen spillover facilitated by the support, strong metal–support interactions leading to metal encapsulation, enhanced chemical reactivity at the metal–support interface, and charge transfer from the metal particle through the support.[2]

State-of-the-art methods for the preparation of heterogeneous catalysts typically involve techniques such as impregnation of metal precursors onto preformed supports or co-precipitation from precursor solutions. While these approaches enable large-scale production, they offer limited control over key metal site properties, such as particle size distribution. As a result, it becomes challenging to attribute the intrinsic catalytic properties to a single type of metal site, unlike in model systems based on well-defined supported metal nanoparticles.[3]

Furthermore, conventional thermal treatments needed during the preparation, such as calcination and reduction, often promote the incorporation of metal species into the support structure. In this context, commonly used supports such as SiO_2, TiO_2, MgO, and Al_2O_3 can lead to the formation of stable metal-support phases, including silicates, titanates, magnesium spinels, and aluminates.[4–8] These metal-containing phases are typically difficult to reduce, often requiring harsh

[a]DTU Physics, Technical University of Denmark, Kongens Lyngby, DK-2800, Denmark. E-mail: egagi@dtu.dk; filro@dtu.dk; icho@dtu.dk; cdda@dtu.dk

[b]VISION, DTU Physics, Technical University of Denmark, Kongens Lyngby, DK-2800, Denmark. E-mail: rbuvi@dtu.dk

[c]Dipartimento Chimica Industriale "Toso Montanari, Università di Bologna, Bologna, 40136, Italy. E-mail: ilenia.giarnieri2@unibo.it; patricia.benito3@unibo.it

[d]DTU Nanolab, Technical University of Denmark, Kongens Lyngby, DK-2800, Denmark

† Electronic supplementary information (ESI) available. See DOI: https://doi.org/10.1039/d5ta03667d

reduction conditions to generate the active catalytic phase. Consequently, this can lead to the coexistence of metal species with distinct chemical nature and reactivity. In this regards, the colloidal synthesis of metal nanoparticles allows the pre-formation of metal (and metal oxides) particles with controlled properties. Afterwards, their incorporation into the support by simple impregnation or physical mixture avoid or minimize the formation of undesired phases, since the interaction between the metal sites and the support are only based on physical adsorption.[9]

Carbon nanotubes (CNTs) represent a class of functional materials characterized by exceptional properties at the nanoscale. Their high mechanical strength, lightweight structure, superior electrical conductivity, and high thermal stability make them highly versatile for applications including electronics, energy storage, structural materials, and healthcare.[10] Aligning with the global energy transition, CNTs are increasingly being explored in energy storage and conversion technologies such as batteries, capacitors, and fuel cells.[11–13]

The production of CNTs is predominantly achieved through chemical vapor deposition (CVD), a method favored for its simplicity, scalability, and cost-effectiveness. CVD typically involves the thermal decomposition of carbon sources, such as ethylene (C_2H_4) or acetylene (C_2H_2), at elevated temperatures in the presence of catalysts, commonly based on iron (Fe), cobalt (Co), or nickel (Ni). Fe is particularly interesting among other transition metals due to its high catalytic activity and stability at high temperatures, where thermodynamic conversions are favored,[14] and due to its crustal abundance.[15]

Within this context, methane (CH_4) decomposition has garnered significant attention due to its dual production of high-purity CO_2-free H_2 and carbon as sole products. The process holds industrial relevance, as it utilizes an inexpensive carbon source and relies on well-established operational units and distribution technologies.[16] CH_4 decomposition is an endothermic reaction conducted at atmospheric pressure and temperatures ranging from 500 to 900 °C. Nevertheless, formation of undesired carbonaceous structures contribute to catalyst deactivation, either through sintering and/or the blockage of active sites caused by carbon encapsulation.

In this work, we explore the catalytic activity of preformed colloidal iron nanoparticles (FeNPs) impregnated on selected supports (SiO_2, MgO, Si_3N_4 and $MgAl_2O_4$). Thus, allowing a fair comparison between pre-formed active sites, the nature of the support and the final morphology of carbon products. By combining both *ex situ* techniques like TEM, STEM-EDS, SEM, XPS, Raman spectroscopy, *in situ* XRD and *in situ* TEM, it was found that the nature of the support greatly affects the catalytic activity in terms of carbon yield and the properties of the final carbonaceous products.

Surprisingly, studies on colloidal iron nanoparticles for CH_4 decomposition are scarce, with reports limited to SiO_2 films and MgO powders.[17–20] Therefore, this study provides a systematic investigation of different support materials. Among them, $MgAl_2O_4$ was the only support that facilitated the formation of micrometer large CNTs. This system was further examined using beam-enhanced *in situ* TEM, revealing that the Fe-based catalyst undergoes reduction and promotes CH_4 cracking, ultimately leading to the formation of base-growth CNTs.

2 Results and discussion

Fig. 1 summarizes the workflow process starting from synthesis, catalysts preparation and testing conditions of the supported colloidal nanocrystals (see details in experimental section). After synthesis and purification, a stable and concentrated FeNPs suspension was obtained. TEM studies (Fig. 2a) indicates a narrow particle size distribution of 6.0 ± 0.5 nm. HR-TEM in Fig. 2c shows a lattice fringe value of 2.0 Å, corresponding to the (110) plane of α-Fe.[21] The sample was prepared by simple drop casting and dried *ex situ* shortly after the synthesis, suggesting that the capping agent protected the nanoparticle from further oxidation in air.

The catalytic experiments were carried out at atmospheric pressure and the catalysts were activated under 50% H_2: he from room temperature up to 750 °C (see further details in experimental section). After 5 minutes, H_2 was switched off and CH_4 was fed. The reaction was kept for 90 minutes.

2.1 Fe/SiO_2

Fig. 3a shows the SEM micrographs of Fe/SiO_2 after reaction, indicating the formation of coral-like roundish structures covering the surface of the catalysts. Backscattered electrons in Fig. 3a shows the presence of large particles with broad size

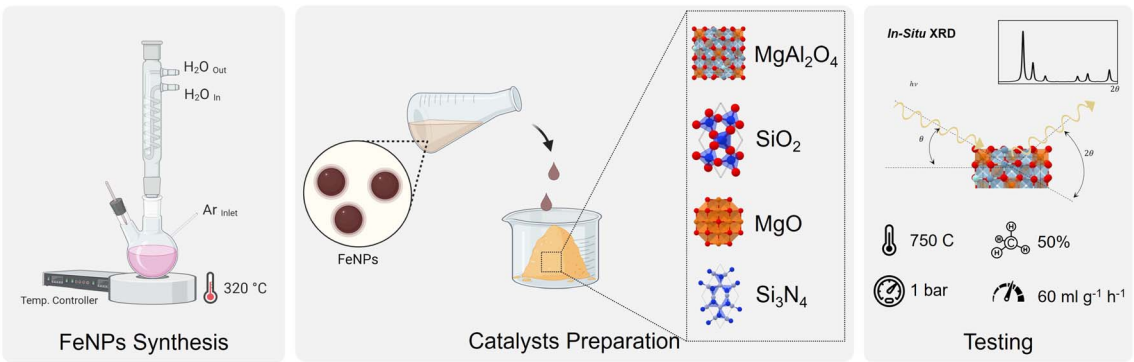

Fig. 1 Schematic representation of the overall process regarding synthesis, preparation and testing of the supported colloidal nanoparticles.

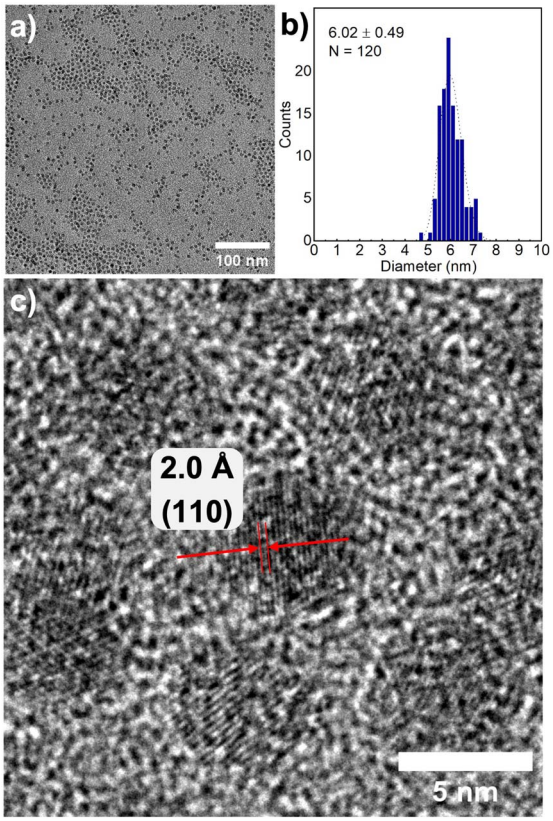

Fig. 2 (a) Low magnification TEM, (b) particle size distribution and (c) HR-TEM of FeNPs.

distribution. This is further verified by STEM-EDS in Fig. 3b and S1.† Large and elongated Fe particles of up to 100 nm are formed, which are completely covered by carbon layers. These fully encapsulated particles are the result of the migration and coalescence of the initial preformed FeNPs, leading to the formation of large and irregular carbonaceous structures known as "nano-onions".[22] Thus, and under the reaction conditions employed in this work, SiO_2 is not an effective support for the stabilization of the Fe colloids towards formation of large CNTs.

Han *et al.* studied the non-oxidative conversion of CH_4 over different silica based Fe catalysts prepared by different approaches. Those ones prepared by fusing methods increased the formation of Fe–O–Si species, leading to increased selectivity towards C^{2+} and aromatics products.[23]Conversely, those ones based on FeO_X particles of weaker interaction were selective towards carbon deposition. Similar results were found by Zhou *et al.*, where the authors claim that CH_4 decomposition proceeded first on Fe^0 sites.[24] After Fe_3C species are formed, supersaturation leads to carbon precipitation and formation of encapsulating graphite layers. Nevertheless, these claims are based on *ex situ* XRD studies.

Wirth *et al.* investigated the phase evolution of Fe nanoparticles during CNT growth *via* C_2H_2 decomposition on 5 nm Fe films. Their study revealed that the formation of Fe_3C as a stable intermediate depends on the initial Fe phase. Specifically, for γ-Fe-rich particles, metallic Fe serves as the intermediate for CNT formation, whereas α-Fe-rich particles promote the formation of carbide species as stable intermediates.[25]

Fig. 3c shows the diffractograms collected *in situ* during CH_4 decomposition. At room temperature (RT), Fe species are not observed, indicating that the crystallite size of initial FeNPs is below the detection limit of the diffractometer. After 15 minutes of reaction, FeNPs are observable as Fe^0, evidenced by the characteristic reflection at 44.5° from the (110) plane of α-Fe (JCPDS 65-4899). After 30 minutes, a transition toward Fe_3C species is observed, remaining stable after 90 minutes (JCPDS 23-1113). These findings align with experimental observations employing both XRD and Mössbauer spectroscopy during CH_4 pyrolysis using ore as iron source.[25,26]

The slight shift in 2 theta values observed between measurements at 750 °C and at room temperature after cooling can be attributed to lattice expansion due to thermal effects, as well as a minor displacement of the catalytic bed within the reaction chamber during the carbon nanostructures formation.

Thus, it is inferred that after Fe_3C formation, metal particles saturation is followed by carbon precipitation. Due to the relatively large particle size promoted by migration and coalescence of preformed FeNPs, encapsulation is promoted and the reaction stops. After cooling down, the reflections characteristics of Fe_3C species are less intense, in agreement with carbon precipitation and the phase-diagram of Fe–C system. The evidence corroborates that FeNPs are first present in a reduced state, prior to Fe_3C formation, highlighting the relevance of *in situ* techniques for unraveling the true state of the active sites under dynamic conditions.

Fig. 3d presents the XPS analysis of the C1s and Fe2p core levels before and after the reaction. The C1s spectrum of the fresh sample reveals three primary peaks at 284.8 eV, 286.3 eV, and 288.2 eV, which correspond to adventitious carbon, C–O, and C═O carboxylic groups, respectively.[27] The presence of surface C–O and C═O species prior to the reaction is attributed to chemisorbed species formed during the decomposition of the metal precursor and the use of capping agents for colloid stabilization.[28,29] After reaction, C1s peak at 284.8 eV becomes more pronounced, corresponding to the encapsulating graphitic carbon covering the catalyst, as observed by SEM and STEM-EDS.

Fe 2p core level of the fresh sample shows peaks between 709.6 and 710.8 eV, corresponding to surfaced oxidized Fe^{2+} and Fe^{3+} species. After reaction, Fe is practically not detected due to the dense encapsulation with graphitic carbon. These findings indicate that the SiO_2 support facilitates significant sintering of FeNPs during the reaction, resulting in the formation of Fe_3C as a stable intermediate during CH_4 decomposition. The carbon nanostructures fully encapsulate the sintered particles, leading to catalyst deactivation and the formation of nano-onion structures, as schematically depicted in Fig. 3e.

2.2 Fe/MgO

Fig. 4a shows the STEM-EDS micrographs of Fe/MgO after reaction. As a main difference, small and dispersed particles of

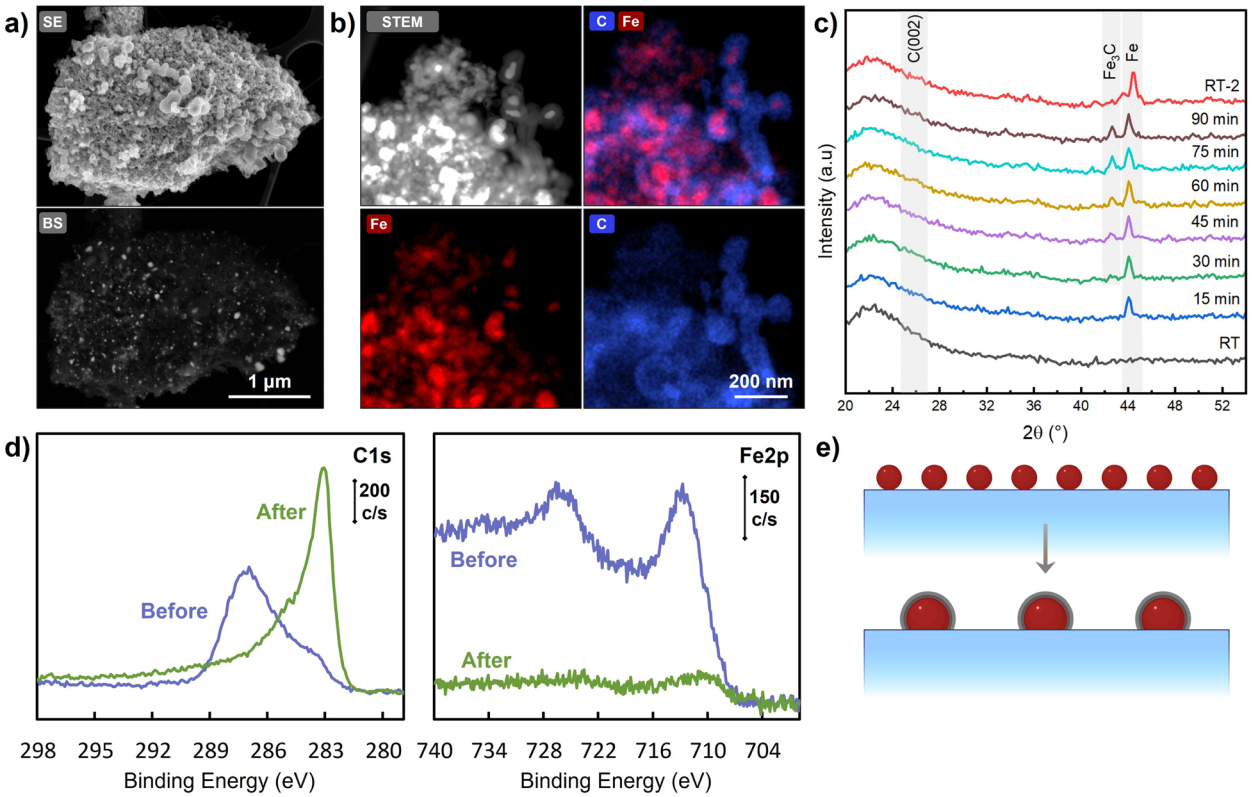

Fig. 3 (a) SEM, (b) STEM-EDS, (c) *in situ* XRD, (d) C1s and Fe 2p XPS and (e) schematic representation of Fe/SiO_2 after reaction.

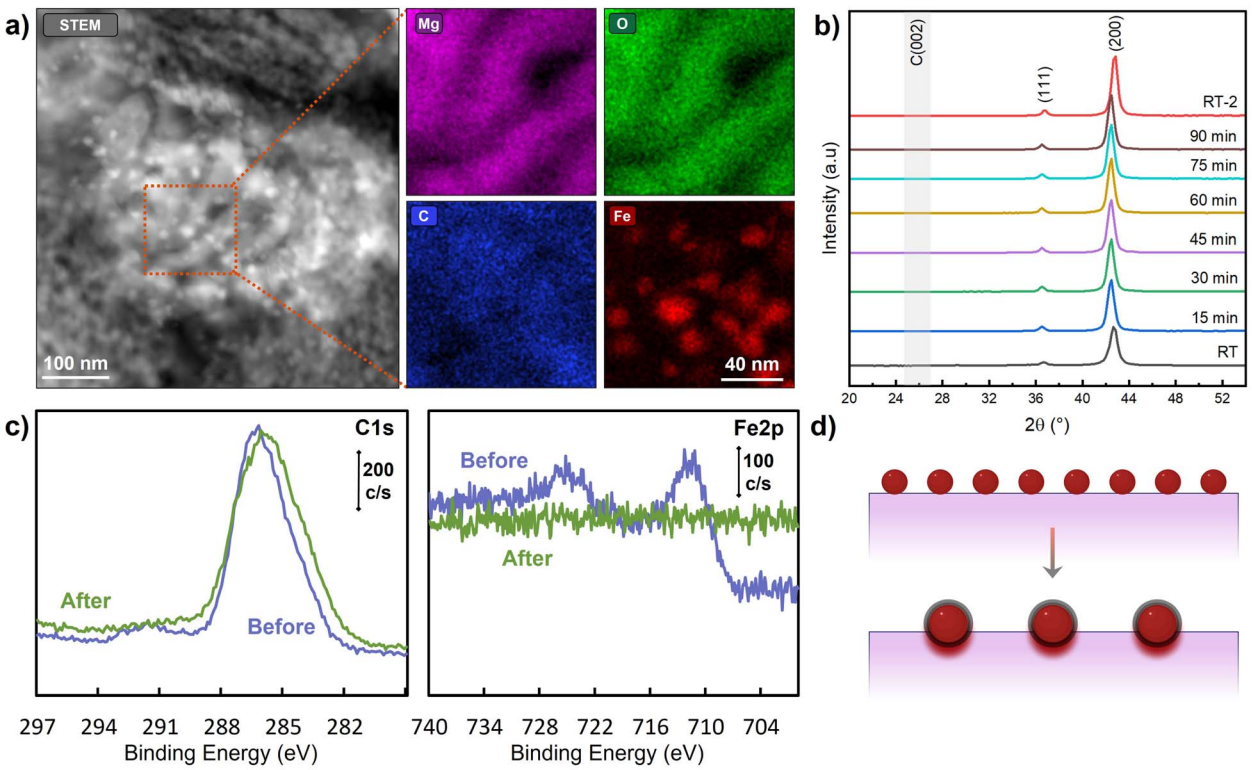

Fig. 4 (a) STEM-EDS, (b) *in situ* XRD, (c) C1s and Fe 2p XPS and (d) schematic representation of Fe/MgO after reaction.

14.4 ± 3.4 nm are observed, confirming by electron dispersive spectroscopy that corresponds to Fe (Fig. S2†). Surprisingly, the particles remained rather stable against migration and coalescence considering that were heated up to 750 °C under H_2 followed by CH_4 decomposition for 90 minutes. Nevertheless, the catalysts was inactive towards formation of large carbonaceous structures, as verified by STEM at both high and low magnification (Fig. S3†).

Fig. 4b shows the diffractograms collected during CH_4 decomposition. The main reflections at 42.7° and 36.7° correspond to the (111) and (200) planes of MgO (JCPDS 4-829). The absence of C (002) graphite reflections suggests the absence of long-range carbon nanotubes formation, or the presence of small amounts of crystalline carbon. The slight shift towards lower 2 theta values between 750 °C and room temperature corresponds to the lattice expansion of MgO due to thermal effects.[30] In addition, Fe phases are not detected due to the formation of well-dispersed amorphous particles and/or with crystallite sizes below the detection limit of the diffractometer.[6]

Ago *et al.* investigated CH_4 decomposition on colloidal Fe nanoparticles (FeNPs) supported on MgO.[19,20] Their study revealed that 10 nm FeNPs were unable to grow CNTs, whereas 4 nm FeNPs facilitated the formation of double- and single-walled CNTs, albeit in very low yields, as identified by TEM. The limited catalytic activity of the 10 nm FeNPs was attributed to their size, suggesting either insufficient CH_4 diffusion under their experimental conditions or inadequate particle reactivity for initiating C–H bond cleavage.

Another possible factor inhibiting CNT formation is the strong metal–support interaction between Fe and MgO. It is well known that Fe particles on MgO are prone to interdiffusion,[31,32] which, particularly at high temperatures, can lead to particle size reduction and the formation of unreduced Fe phases. However, under our experimental conditions, this effect is unlikely, as FeNPs exhibited growth from an initial size of 6.02 ± 0.49 nm to 14.4 ± 3.4 nm.

Topsøe *et al.* investigated the effect of metal–support interactions in the Fe–Mg–O system, demonstrating that iron diffusion into the MgO structure is strongly promoted at high temperatures, regardless of metal loading.[33] Subsequent studies further confirmed that Fe diffusion leads to the formation of formal Fe–O–Mg bonds between Fe nanoparticles (FeNPs) and the support, enhancing both dispersion and thermal stability.[34–36]

A key distinction from traditional catalyst preparation methods is that preformed FeNPs exhibit only weak interactions with the catalyst surface. Therefore, the final particle size in this study is determined by a balance between partial sintering and stabilization *via* subsurface Fe diffusion into the MgO support. This final size does not favor the growth of extended CNT structures. Instead, partial CH_4 decomposition results in surface encapsulation of the metal sites. Similar behavior has been observed when using other carbon precursors, such as C_2H_2 and C_2H_4.[37]

To gain further insights into the chemical state of the catalyst before and after reaction, Fig. 4c presents the XPS spectra of the C1s and Fe 2p core levels. The C1s signal remains nearly constant, attributed to adventitious carbon from the environment. The Fe 2p spectrum exhibits a distinct peak at 710.6 eV, corresponding to oxidized $Fe^{2+/3+}$ species. However, after the reaction, this peak disappears, indicating FeNP encapsulation.

High-resolution TEM further supports these findings (Fig. S4†). The images reveal the formation of FeNPs smaller than 15 nm. Notably, these nanoparticles are uniformly encapsulated by well-defined carbon layers, as confirmed by the presence of lattice fringes at 3.4 Å, corresponding to the (002) plane of graphitic carbon. Both detached and anchored FeNPs are observed, where carbon structures are predominantly encapsulating FeNPs with short-range ordering.

The combined results from HR-TEM, STEM-EDS, *in situ* XRD, and XPS indicate that FeNPs are thermally stabilized under reaction conditions, exhibiting significantly less sintering compared to Fe/SiO_2 and becoming encapsulated by graphitic carbon.

2.3 Fe/Si_3N_4

Fig. 5a presents the STEM-EDS micrographs of Fe/Si_3N_4 after the reaction. At first glance, the presence of very small nanoparticles is evident, with sizes ranging from approximately 4 to 9 nm (further details are provided in Fig. S5†). Energy-dispersive spectroscopy (EDS) analysis confirms the iron composition of these nanoparticles (Fig. S6†).

STEM-EDS mapping indicates a strong correlation between oxygen and silicon, suggesting the presence of a silicon oxide phase. Notably, Fe/Si_3N_4 seems to be covered by a shell-like structure. Elemental mapping further reveals that this shell is composed of nitrogen and carbon, in agreement with the lower contrast in HAADF mode consistent with the lower atomic numbers of these elements.

Fig. S7a† shows a low-magnification TEM of the spent catalyst. Unlike Fe/MgO, which exhibits clear carbon encapsulation and the formation of nanometric carbon structures, Fe/Si_3N_4 does not show evidence of carbon deposition. Fig. S7b† displays a HR-TEM micrograph of an individual supported nanoparticle. No carbonaceous structures are observed, and the measured lattice fringe spacing of 3.0 Å corresponds to the (220) plane of partially oxidized $Fe^{2+}Fe^{3+}O_4$ magnetite.[38] Similar to Fe/MgO, *in situ* XRD does not reveal any detectable C (002) graphite reflections or iron-containing phases (Fig. 5b). Thus, suggesting that the iron particles are rather stable and below the detection limit of the diffractometer, and the absence of carbon formation.

The diffraction peaks observed in the fresh Fe/Si_3N_4 catalyst at $2 = 23°$, 32.5°, and 46.5° can be attributed to the (110), (002), and (122) planes of $-Si_3N_4$, respectively. However, the most intense reflections of this phase, located at 20.6° and 31° 2 and corresponding to the (111) and (221) planes (ICSD 6004), are not clearly observed. A similar analysis excludes the presence of $-Si_3N_4$, as its most intense reflection at 27.1° 2 (220) (ICSD 8263) is also absent. Interestingly, these additional diffraction peaks are present only in the fresh catalyst after FeNPs deposition and disappear after reaction and subsequent cooling to room temperature. At the industrial scale, SiN is typically produced

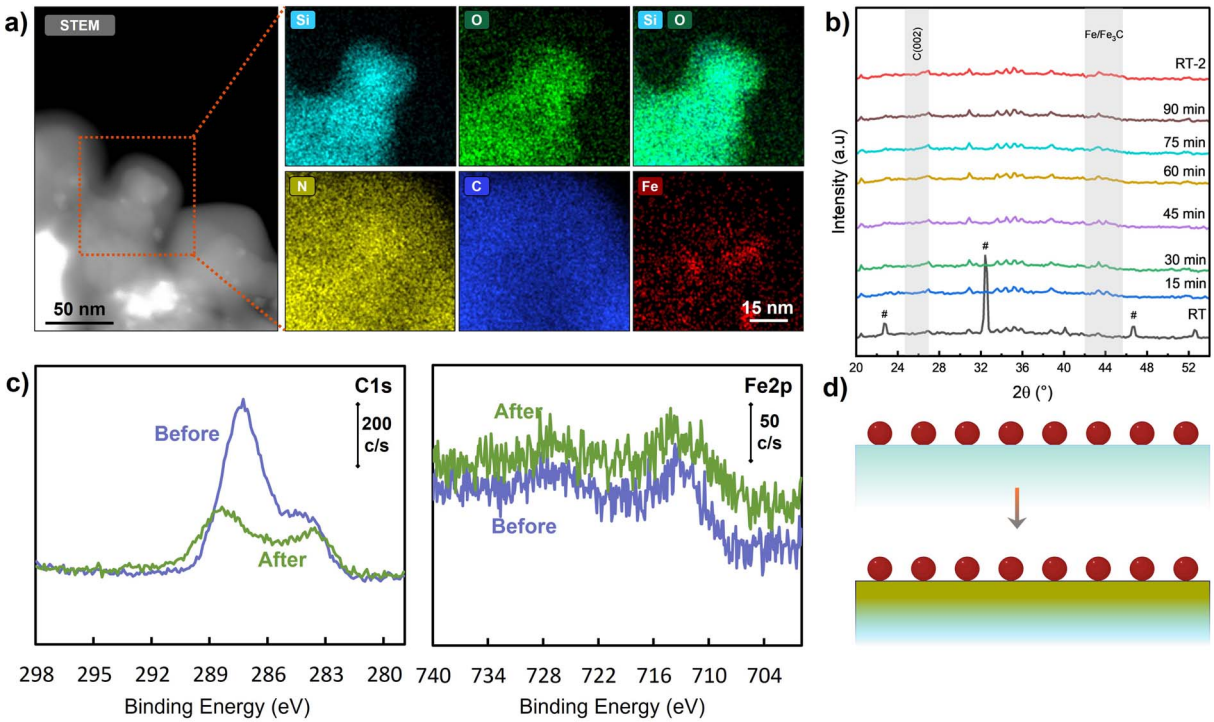

Fig. 5 (a) STEM-EDS, (b) *in situ* XRD, (c) C1s and Fe 2p XPS and (d) schematic representation of Fe/Si_3N_4 after reaction.

via nitridation of silicon or carburization of silicon oxide under nitrogen atmosphere. Therefore, although the exact origin of these reflections cannot be fully determined, we infer that they may arise from residual precursor species remaining from the SiN synthesis process.

The XPS spectra of the sample before and after reaction are shown in Fig. 5c. Prior to reaction, the C1s core-level spectrum exhibits two distinct peaks at 284.8 eV and 287.4 eV, corresponding to adventitious carbon and adsorbed C=O species. After reaction (*i.e.*, reduction under H_2 followed by exposure to CH_4 at 750 °C for 90 minutes), two carbon species appear at 284.3 eV and 288.5 eV. The first is again attributed to adventitious carbon, while the second, at a relatively higher binding energy, is assigned to surface-bound C–N=C species, as discussed below.

To gain further insights into nitrogen-containing species, Fig. 6a presents the XPS spectra of the N1s core level before and after reaction. The contribution at 400.7–401.8 eV is associated with silicon oxynitride (Si–N–O_2 and Si_2–N–O) species, commonly found in industrially synthesized silicon nitride supports.[39] A second peak, appearing at 397.5–397.8 eV, is attributed to both N–Si bonds from the silicon nitride structure and C–N=C species. The total nitrogen concentration at the surface remained practically the same (17.9% at. before reaction and 17.5% after reaction). Nevertheless, the contribution at 397.5–397.8 eV increases from 5.3% to 7.2% after reaction. Given that the reaction conditions were nitrogen-free, the increase of N–Si bonds from the silicon nitride structure and C–N=C species would suggest a slight segregation of nitrogen from the silicon nitride support to the surface or the formation of carbon nitrides species after methane cracking.

Fig. 6b shows additional HR-TEM images of the Fe/Si_3N_4 catalyst, illustrating the amorphous nature of the support, in agreement with the XRD results. Some isolated crystalline regions are observed (Fig. 6c), with lattice fringes measuring 3.9 Å, corresponding to the (110) plane of Si_3N_4. Fig. 6d reveals a distinct phase with a lattice fringe spacing of 3.5 Å, attributed to the (002) plane of triazine (C_3N_3), a structure composed of stacked sheets of sp^2-hybridized carbon and nitrogen atoms.[40]

Previous studies have reported the formation of carbon nitride films through chemical vapor deposition (CVD) using CH_4, H_2, and NH_3 on flat Si wafers. Regardless of decomposition conditions, the most probable structure is α-C_3N_4, which exhibits the same lattice plane distances as those observed in HR-TEM. However, in the present case, the proposed phase is a solid solution of $Si_XN_YC_Z$, in which carbon occupies interchangeable nitrogen sites.[41] AlShibane *et al.* previously reported the catalytic activity of amorphous silicon nitride composites for CH_4 cracking.[42] While these materials exhibit low catalytic activity, the nature of the carbon deposits was not characterized to verify the formation of C_XN_Y species.

In this context, it has been shown that the basic properties of Si_3N_4 can enhance alkane dehydrogenation reactions.[43,44] More recently, Si_3N_4 has been demonstrated as an effective support for zinc-based complexes that promote propane dehydrogenation to propylene, contrasting with the inertness of SiO_2. The active sites are attributed to the Lewis basicity of nitrogen species, which facilitates heterolytic C–H bond activation. Therefore, Si_3N_4 could play a role in promoting C–H cleavage of

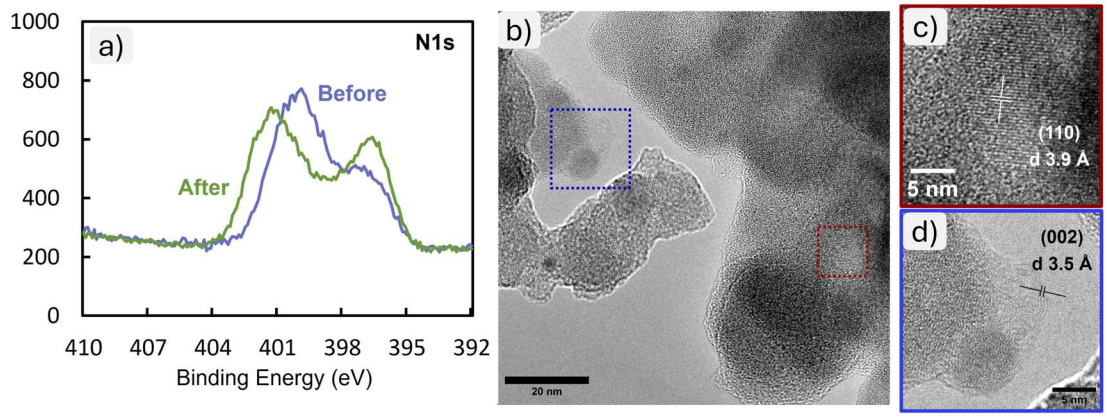

Fig. 6 (a) STEM-EDS, (b) *in situ* XRD, (c) C1s and Fe 2p XPS and (d) schematic representation of Fe/SiN after reaction.

methane and stabilizing intermediates formed during the cracking process.[45] However, further studies are needed to fully elucidate the underlying mechanism.

Therefore, the present results suggest that CH_4 can be partially decomposed on the support, leading to the formation of a surface layer of carbon nitride. Iron silicide species were not detected. The preformed FeNPs remain stable on the Si_3N_4 support without undergoing carbon encapsulation, as indicated by STEM-EDS, HR-TEM, and XPS (Fig. 5d).

2.4 Fe/$MgAl_2O_4$

$MgAl_2O_4$ spinel oxide is recognized as an excellent support due to its high chemical and thermal stability under harsh reaction conditions. This material has been extensively utilized for Pt, Co, and Ni nanoparticles in applications such as methanol oxidation, as well as dry and steam CH_4 reforming. The superior stability of $MgAl_2O_4$ is attributed to the strong interaction between the supported metal nanoparticles and surface oxygen atoms within the spinel structure.[46,47] However, its use in CH_4 decomposition has been scarcely explored.[48] Previous studies have primarily focused on Ni-supported nanoparticles, demonstrating enhanced stability against deactivation due to the strong stabilization of metal particles.[49–54]

Fig. 7a presents SEM micrographs of Fe/$MgAl_2O_4$ catalysts after reaction, revealing abundant CNT formation with a broad diameter distribution. Backscattered electron imaging verifies the presence of large metal particles, resulting from the sintering of the initial FeNPs. This observation is further supported

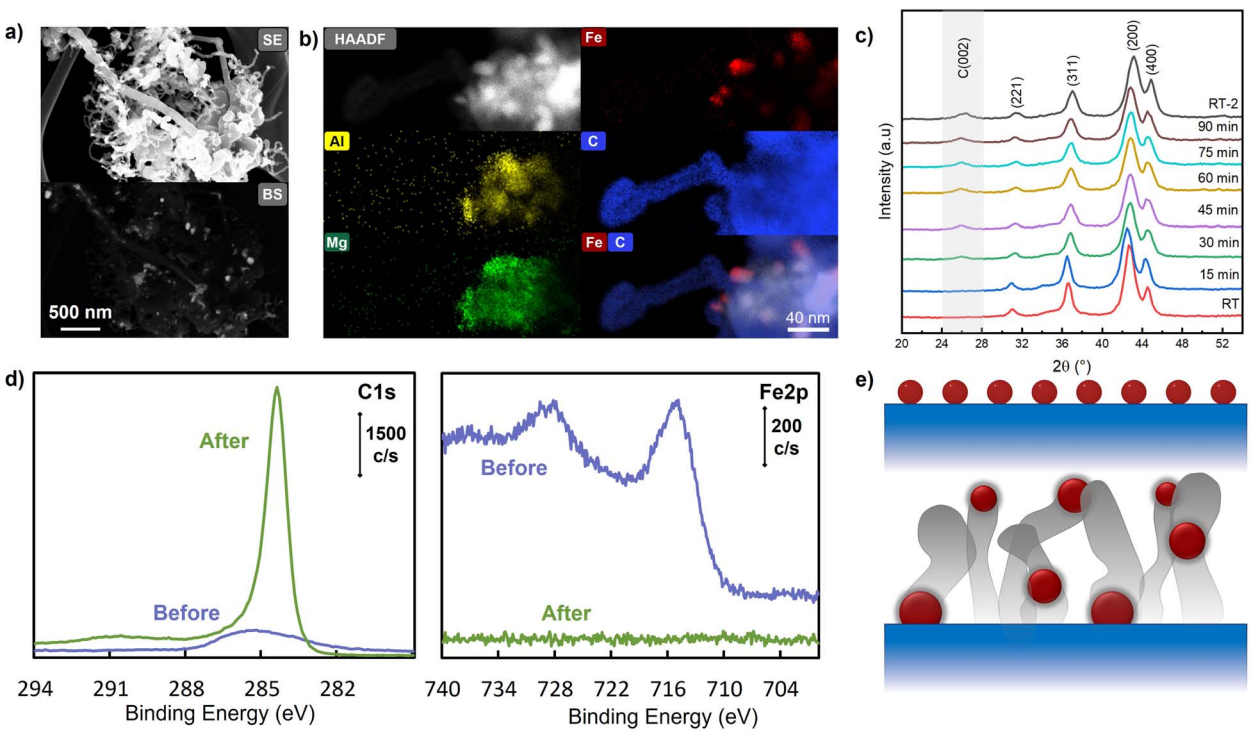

Fig. 7 (a) SEM, (b) *in situ* XRD, (c) C1s and Fe 2p XPS and (d) schematic representation of Fe/$MgAlO_x$ after reaction.

by STEM-EDS microscopy (Fig. S8†), which reveals micrometer-long CNTs containing elongated Fe nanoparticles encapsulated within their tubular structures. Additionally, particles of varying sizes, including larger aggregates up to 100 nm and smaller supported particles below 10 nm, are observed. As shown in Fig. 7b and the corresponding spectra in Fig. S9,† it is also verified the formation of base-growth CNTs, with FeNPs remaining anchored to the spinel support. This anchoring prevents detachment and mitigates significant sintering.

X-ray diffractograms collected *in situ* indicate that the $MgAl_2O_4$ spinel structure remains intact (Fig. 7c). The characteristic reflections at 30.9°, 36.6°, 42.7°, and 44.5° correspond to the (221), (311), (200), and (400) planes, respectively (JCPDS 21-1152).[55] Similar to Fe/MgO, a slight shift toward lower 2θ values is observed, attributed to lattice expansion due to thermal effects. However, after 30 minutes of reaction, a slight positive shift emerges, likely resulting from vertical sample expansion caused by CNT growth. This interpretation is consistent with the appearance of the characteristic reflection at 25.9°, corresponding to the (002) plane of graphitic carbon. Fig. S10a and b† illustrate the temporal evolution of the C(002) plane and a photograph of the sample post-reaction, highlighting the expansion of the catalytic bed inside the holder. The potential formation of FeC_X species cannot be ruled out due to the strong reflections of the support and the overlap of diffraction peaks associated with $MgAl_2O_4$ and Fe-containing species.

The chemical states of the catalyst before activation and after reaction were analyzed by XPS (Fig. 7d). The C1s core level spectrum reveals a significant increase in carbon content following the reaction. Before exposure to CH_4, the Fe 2p core level displays peaks at 709.6 eV and 710.8 eV, corresponding to surface Fe^{2+} and Fe^{3+} species, respectively. After the reaction, Fe 2p signals are no longer detectable. This could be related to a dilution effect of the FeNPs contained between the large amount of formed CNTs, but also agrees with STEM-EDS observations indicating complete encapsulation of FeNPs by carbonaceous structures after CH_4 cracking.

Therefore, the balance between metal–support interaction and reactivity led to the formation of active Fe nanoparticles, promoting the formation of long-range CNTs structures following both a tip- and a base growth mechanism (Fig. 7e).

2.5 Raman spectroscopy of carbon nanostructures

Raman spectroscopy is a crucial tool for characterizing carbonaceous structures, including carbon nanotubes and graphene-based materials. This technique identifies structural features by analyzing vibrational modes. In carbon nanotubes, the G-band (approximately 1580 cm^{-1}) corresponds to the stretching of C–C sp^2 bonds in graphitic materials, serving as an indicator of crystallinity and being sensitive to strain effects in multilayered structures. The D_1-band (approximately 1350 cm^{-1}) is associated with structural disorder or defects within the carbon framework, arising from impurities that induce sp^3 hybridization and disruptions in sp^2 bonding along the nanotube sidewalls. A higher intensity of the disordered D_3 (1475 cm^{-1}) and D_4 (1217 cm^{-1}) bands typically corresponds to a greater degree of short-range disorder, such as carbon encapsulation or the deposition of defective graphene layers.[56,57]

The intensity ratio I_{D_1}/I_G provides a quantitative measure of structural disorder in carbon materials, where higher values indicate increased structural defects. Additionally, second-order bands above 2250 cm^{-1}, such as the G′ (or 2D) band at 2700 cm^{-1}, are often enhanced in carbon nanotubes and serve as markers of long-range order.

Fig. 8a and b present a representative Raman spectrum and the mean I_{D_1}/I_G values obtained from six independent spectra collected at different locations, respectively. As observed, Fe/$MgAl_2O_4$ exhibits the highest degree of crystallinity, consistent with previous characterizations indicating the formation of long-range, well-ordered carbon nanotubes. Among all samples, Fe/MgO displays the highest degree of disorder. However, unlike Fe/SiO_2 and Fe/Si_3N_4, the Fe/MgO spectrum features a prominent G′ band and lacks significant contributions from the D_3 and D_4 bands. Based on previous characterizations, this suggests that the observed disorder primarily arises from strain

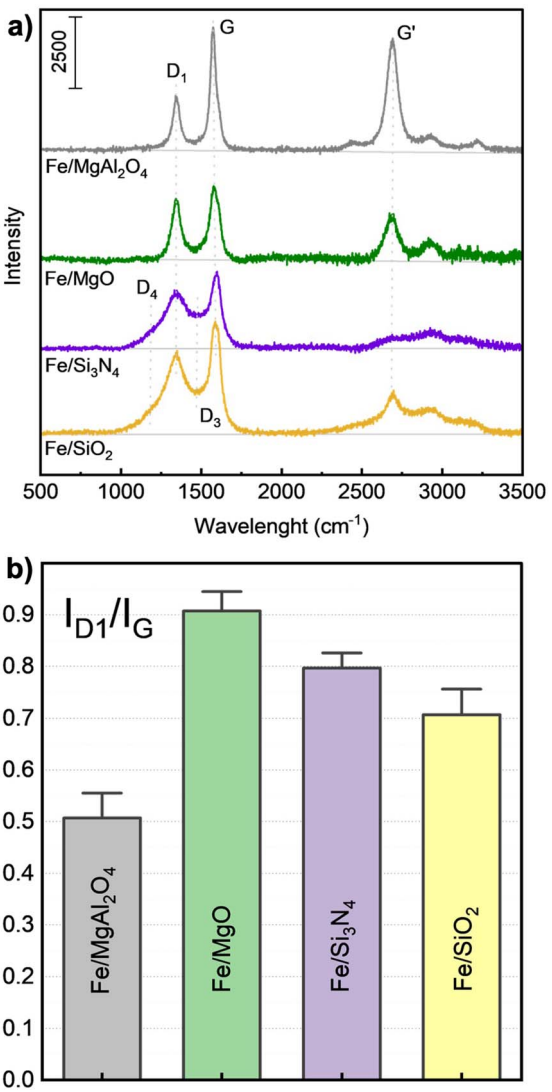

Fig. 8 (a) Raman spectra and (b) I_{D_1}/I_G values of spent catalysts.

effects due to the curvature of relatively small, encapsulated Fe nanoparticles rather than significant structural defects.

Fe/SiO_2 exhibits a lower I_{D_1}/I_G ratio compared to Fe/Si_3N_4. Nevertheless, both spectra display similar contributions from the D_3 and D_4 bands, indicating the presence of impurities such as ionic species from the support, metal nanoparticles, interstitial defects, or structural disorder induced by oxygen-containing functional groups (*e.g.*, carbonyls).[58,59]

These results agree with the previous characterizations and illustrate how the morphology and structural characteristics of carbon materials can be rapidly inferred from a Raman spectrum, assessing the quality and nature of carbon-based nanostructures.

2.6 *In situ* TEM studies: $Fe/MgAl_2O_4$

Based on previous results, $MgAl_2O_4$ was identified as the only support capable of promoting the growth of micrometer-long CNTs. Consequently, *in situ* TEM experiments were conducted to gain insights into the growth mechanism of these nanostructures. Preformed FeNPs were drop-cast onto the $MgAl_2O_4$ support, which had been pre-deposited on a commercial microchip (see the experimental section for details).

The specimen was heated under 1 mbar H_2 from room temperature up to 700 °C. Despite 3 hours of treatment, selected area electron diffraction (SAED) patterns showed no evidence of metallic Fe formation and predominantly the diffractions of the $MgAl_2O_4$ support (Fig. S11†). Subsequently, CH_4 was introduced increasing the total pressure to 2 mbar. However, even after 2 hours of exposure, no CNTs formation was observed.

Yoshida *et al.* were the first to report CNTs growth on Fe particles supported on SiO_2 at 600 °C and 0.1 mbar of C_2H_2.[60] Their study demonstrated that CNTs growth was driven by fluctuating Fe_3C nanoparticles, where carbon atoms diffused through the bulk of the carbide phase. A key distinction in their work was the use of C_2H_2, a carbon source with significantly lower activation energy due to the high reactivity of its triple C–C bond compared to CH_4. Similar findings were reported by Wirth *et al.*, who also used C_2H_2 at 0.01 mbar.[25] Their results indicated that the formation of iron carbide is not necessarily a prerequisite for CNTs growth, as the process strongly depends on the specific iron phase present during the reaction.

Using CO as the carbon source, He *et al.* demonstrated the base-growth of single-walled CNTs on a Fe–Cu/MgO catalyst at 690 °C and 6.9 mbar.[61] However, it was not confirmed whether the active catalyst phase was metallic Fe or an FeC_X phase under dynamic conditions. Later, Liu *et al.* verified the complete reduction of 20 nm Fe_2O_3 nanoparticles after pretreatment at 700 °C in 4 mbar of H_2 for 2 hours. Their study also indicated that Fe_5C_2 was the most stable phase when using a syngas mixture (CO/H_2) at 6 mbar.[62]

Although several studies have explored by *in situ* TEM the growth mechanisms of CNTs on Fe-based catalysts using CO or acetylene at both low and atmospheric pressures, CNTs growth with CH_4 as the carbon source has not been reported.[63,64] As expected, CNTs growth and kinetics are highly dependent on parameters like temperature, partial pressure and nature of the carbon source.[65] Therefore, it is inferred that at low CH_4 partial pressures, Fe nanoparticles are unable to effectively activate C–H bonds. In contrast, under atmospheric pressure conditions, iron oxides have been shown to directly activate CH_4, leading to the formation of carbon structures with a carbide phase as a stable intermediate.[66]

To facilitate CH_4 decomposition, the electron beam was condensed on the microscope screen (see experimental section for details). The enhancement of chemical reactions under electron beam irradiation in *in situ* TEM has been previously documented. This can be related to several factors like heating effect, defects formation, charging of the particle, or excitation of surrounding gases.[67] For example, the electron beam has been shown to accelerate the oxidation of model copper nanoparticles due to promoted diffusion of Cu^{+1} species towards the outer shell of the particles.[68] Similarly, the electron beam can greatly promote the oxidation of iron nanoparticles due to enhanced mass transport of oxygen species across the outer shell.[69] Similarly, the enhanced formation of SiO_{2-X} layers on perovskites electrodes as also been reported.[70,71]

Upon focusing the electron beam on the studied region, CNTs growth was observed. As shown in Fig. 9, no metal nanoparticles were detected at the tips of the CNTs, indicating a base-growth mechanism. This suggests that FeNPs remained anchored to the $MgAl_2O_4$ support, facilitating CNTs growth. The internal structure of the nanotubes revealed graphene layers forming within the tubes. These features, previously observed in Ni catalysts, have been attributed to the dynamic elongation of metallic sites during growth, followed by contraction due to cohesive forces.[72] It is inferred that the catalytic decomposition of CH_4 is promoted by C–H bond cleavage under electron beam irradiation. However, quantifying electron beam-induced local temperature changes or promoted excitation of surrounding reactive gases remains a challenge and a field of current development.[73]

For comparison, FeNPs were also deposited on Au grids coated with Lacey carbon. Using a custom-made holder, the grid was placed in the *in situ* XRD chamber and heated from room temperature to 700 °C at a rate of 10 °C min^{-1} under a 50 ml min^{-1} He flow. Once the reaction temperature was reached, a 35% CH_4 mixture was introduced, and the reaction proceeded for 1 hour. Fig. S12† presents TEM images before and after the reaction, where CNTs formation were observed following exclusively a tip-growth mechanism. The CNTs diameters correlated with the sizes of FeNPs located at their tips. The elongated shape of the metallic tips suggests that under these reaction conditions, the FeNPs were in a molten state, enabling tip-growth CNTs formation.

These findings highlight the importance of selecting an appropriate catalyst support that enables FeNPs anchoring without deactivation due to sintering or encapsulation, thereby promoting the growth of large CNTs. This is further discussed in the section "metal–support interaction and role of the support", where we demonstrate that the oxyphilic character of the support and the anchoring of metal sites significantly influence both the stabilization of the nanoparticles and the resulting CNT growth mode.[74] The results suggest that CH_4

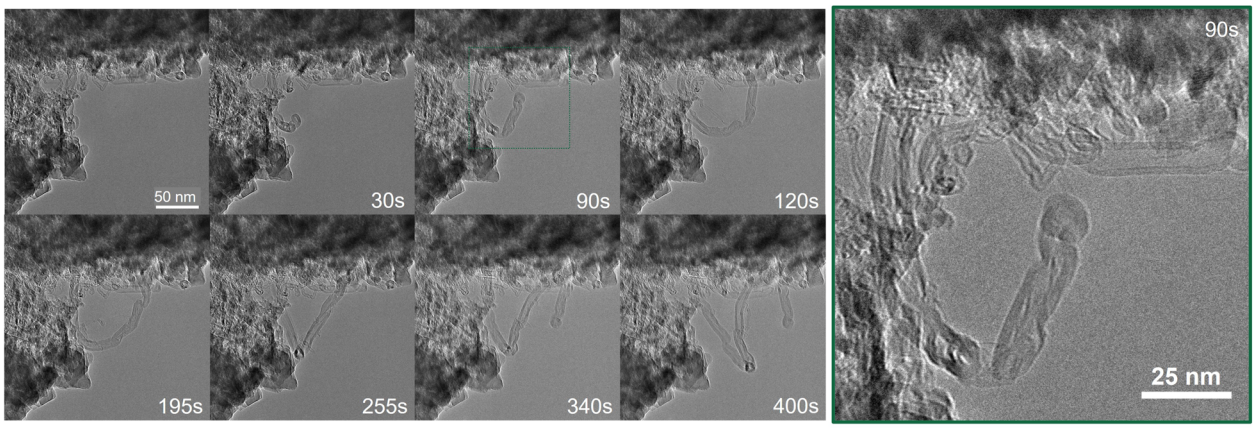

Fig. 9 Beam-enhanced *in situ* TEM of FeNPs supported on $MgAl_2O_4$. Time frame indicated in seconds.

decomposition is significantly influenced by reaction conditions, including CH_4 partial pressure, catalyst phase, and electron beam-induced effects. While $Fe/MgAl_2O_4$ enables CNTs growth under beam-enhanced conditions, further investigations are required to elucidate the exact role of electron irradiation. Nevertheless, these observations are in agreement with the observed activity of $Fe/MgAl_2O_4$ at atmospheric pressure, where a combination of encapsulating carbon, base- and tip-growth CNTs were observed.

2.7 Metal–support interaction and role of support

In the context of heterogeneous catalysis, migration refers to the movement of metal nanoparticles across the support surface, often through Brownian-like motion. This migration enables nanoparticles to come close enough to merge. Coalescence is the process where two or more nanoparticles combine to form a larger particle once they encounter each other on the support surface. Migration and coalescence together lead to particle growth by directly combining preformed nanoparticles.[75,76]

This process differs from Ostwald ripening, where growth occurs indirectly through the movement of atomic or molecular species (adatoms) rather than whole nanoparticles. In Ostwald ripening, smaller particles dissolve and release atoms, which then redeposit onto larger particles, driven by differences in surface energy. This results in the gradual growth of larger particles at the expense of smaller ones without particle migration.[77] While both processes lead to larger particle formation, migration and coalescence involve entire nanoparticles moving and merging, whereas Ostwald ripening relies on atom-by-atom transfer.

The formation of large metallic particles due to migration and coalescence of preformed metal nanoparticles is influenced by factors like temperature, particle size, and metal–support interaction. Higher temperatures increase the mobility of nanoparticles, promoting their migration and potential coalescence when particles come into close proximity. Smaller particles tend to be more mobile due to their high surface energy, leading them to migrate more readily than larger particles. Additionally, the interaction between the metal and the support material plays a crucial role; weak metal–support interactions can facilitate particle mobility, while stronger interactions can stabilize particles and reduce the likelihood of migration and coalescence.

Specific surface area is an important factor that can influence the sintering behavior of metal nanoparticles. However, the catalyst that exhibited the most pronounced sintering, Fe/SiO_2, was supported on the material with the highest specific surface area (according to the supplier, SiO_2: 200 $m^2\ g^{-1}$, MgO: 7 $m^2\ g^{-1}$, Si_3N_4: 113 $m^2\ g^{-1}$. For the $MgAl_2O_4$ spinel, the SSA measured by N_2 sorption is 148 $m^2\ g^{-1}$. Therefore, under the harsh reaction conditions applied in this study (750 °C, reducing atmosphere, 2 hours), the influence of surface area on preventing the sintering of the preformed colloids can be reasonably excluded.

In view of the previous results, it is clear that the nature of the support greatly influences the final type of carbon nanostructures, where other factors like temperatures, reaction conditions and characteristics of preformed FeNPs remained constant. Meanwhile SiO_2 led to large migration, coalescence and sintering; other supports like MgO and Si_3N_4 preserved the nanometric size of FeNPs, even under harsh conditions. Interestingly, $MgAl_2O_4$ showed an intermediate behavior, limiting the degree of sintering but promoting the formation of long-range carbon nanotubes.

The oxyphilic character of catalytic supports plays a crucial role in determining the stability of supported metal nanoparticles, particularly under harsh thermochemical conditions. A key factor is the enhancement of metal–support interactions through the formation of formal metal–oxygen bonds, which reduces nanoparticle mobility and sintering. A relevant descriptor in this context is the adhesion energy, as proposed by Campbell *et al.*, which depends on the surface oxygen density, the chemical nature of the support, and the size and composition of the metal nanoparticles. In addition to metal–oxygen bonding, certain oxyphilic supports such as CeO_2 or TiO_2 can stabilize nanoparticles *via* oxygen vacancies. These defective sites are generally considered nucleophilic and can act as anchoring or stabilizing centers for metal particles.[78]

In contrast, nitrogen-containing supports such as Si_3N_4, BN, and C_3N_3 lack surface oxygen and are therefore less effective at stabilizing metal nanoparticles through conventional metal–oxygen bonding. However, these materials can be engineered to contain nitrogen vacancies, which serve as effective anchoring sites for metal species. Additionally, they offer the potential for the formal incorporation of metal single atoms into their lattice structure, providing alternative stabilization pathways beyond conventional metal–support interactions.[79–81]

Campbell *et al.* correlated experimental observations with thermodynamical calculations to predict the strength of metal–support interactions.[82–84] In this model, the chemical potential of hemispherical metal nanoparticles supported on model planar surfaces are described by two predictors: the surface energy (γ_{metal}) of the metal particle (which is highly dependent on the particle size) and the adhesion energy (E_{adh}), dependent on the oxophylic nature of the support (Fig. 10).

The predicted E_{adh} agrees with expected trends, where adhesion energy per surface oxygen atom increases with decreasing tendency of certain chemical compounds to form oxides, *i.e.*, the weaker the oxidic support holds its oxygen atom, the larger is the adhesion energy per mole of surface oxygen atoms.

The adhesion energies were calculated considering the same initial FeNPs size, and chemical nature of the metal nanoparticle. Values of enthalpies of reduction were taken from literature and normalized per oxygen atom.[82–85] As expected, SiO_2 holds the lowest adhesion energy (-27 kJ mol^{-1} O) leading to a poor FeNP–SiO_2 interaction and thus, large migration and coalescence. On the other hand, MgO and $MgAl_2O_4$ give rise to values of 79 kJ mol^{-1} O and 102 kJ mol^{-1}, respectively. Thus, predicting a higher interaction within the preformed Fe colloids and the support, in agreement with the experimental observations. Therefore, it is expected that highly oxophylic supports (*e.g.*, spinel $MgAl_2O_4$, perovskites and CeO_2) can preserve the nanometric size of preformed colloids and show promising activity towards CH_4 cracking at high temperatures. Nevertheless, it should be mention that this is a simplified model that does not predict simultaneous chemical transformations due to, *e.g.*, preferential diffusion of Fe into the MgO, Fe carbides formation under CH_4 decomposition or large particle size changes due to thermal effects.

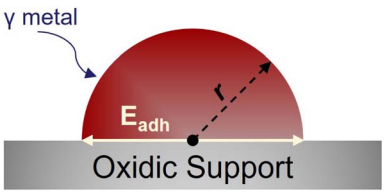

$$E_{adh\ (per\ mole\ surface\ oxygen\ atoms)}$$
$$E_{adh} = -0.344\Delta H_{red\ support} + 286\ kJ\ mol\ 0^{-1}$$

Fig. 10 Schematic representation of a metal nanoparticle on a generic oxidic support, and the estimation of its adhesion force. Adapted with permission from ref. 83. Copyright 2017 American Chemical Society.

3 Conclusions

Methane decomposition into carbon and hydrogen requires suitable catalysts due to the high temperatures and severe reaction conditions. Iron nanoparticles (FeNPs) are widely studied for this process, but they suffer from deactivation due to sintering and/or encapsulation under harsh conditions.

This study explores pre-formed FeNPs deposited on various supports as model catalytic sites for methane decomposition. The results enable the selection of an optimal support for the growth of micrometer-scale carbon nanotubes (CNTs), providing insights into the active phase and growth mechanisms under controlled conditions.

Fe/SiO_2 formed FeC_3 during methane decomposition, but severe sintering and carbon encapsulation led to complete deactivation. Fe/MgO was rapidly deactivated by encapsulation, yet the support stabilized FeNPs, preventing extensive sintering even under high temperatures and reducing conditions. Surprisingly, FeNPs were also stabilized on Si_3N_4, though carburization led to the formation of a protective carbon nitride surface layer.

The most active catalyst for CNTs formation was Fe/$MgAl_2O_4$. However, the harsh reaction conditions yielded a mixture of carbon structures, including nanofibers, multiwalled CNTs, and encapsulated FeNPs. Beam-enhanced *in situ* TEM confirmed a base-growth mechanism, with FeNPs remaining anchored to the support.

Despite using identical FeNPs, the oxophylic nature of the support s a key descriptor influencing catalytic activity in terms of carbon yield and the nature of the formed nanostructures. $MgAl_2O_4$ demonstrated an optimal balance between Fe–O–Mg–Al interactions and nanoparticle reactivity, making it an excellent support for CO_2-free H_2 and CNTs formation *via* CH_4 decomposition.

4 Experimental section

All chemicals were used as received without any further purification. MgO, SiO_2 Davisil® and Si_3N_4 were obtained from Sigma-Aldrich, Germany.

The $MgAl_2O_4$ support was synthesized *via* the co-precipitation method with a Mg^{2+}/Al^{3+} molar ratio of 2 : 1. To obtain 5 g of the calcined catalyst, an aqueous solution (114 ml) with a total molarity of 1 M was prepared, containing 19.9 g of $Mg(NO_3)_2 \cdot 6H_2O$ (99%) and 14.5 g of $Al(NO_3)_3 \cdot 9H_2O$ (≥98%). This solution was added dropwise into 228 ml of a 1 M $Na_2CO_3 \cdot 10H_2O$ (99%) solution (65.2 g) at 60 °C under constant stirring. The pH was maintained at 10.5 by the controlled addition of 3 M NaOH (approximately 200 ml). All reagents were purchased from Sigma-Aldrich. The resulting precipitate was aged for 1 h under the same synthesis conditions, subsequently filtered, washed until reaching a neutral pH, and dried overnight at 60 °C. The dried material was then subjected to calcination in static air at 800 °C for 12 h, employing a heating rate of 10°C min^{-1}.

Octadecene (99%), oleic acid (70%, technical grade) was purchased from Sigma-Aldrich, Germany. Iron oxide hydroxide

(FeO(OH), 99%) was obtained from Carl Roth, Germany. Acetone was obtained from Honeywell Riedel-de-Haën, Germany.

4.1 Synthesis of iron nanoparticles (FeNPs)

Before synthesis, all glassware was cleaned with aqua regia, thoroughly rinsed with distilled water, and dried overnight at 100 °C to guarantee a clean glass surface. The size selected FeNP were prepared following a one-pot heating-up approach based on the thermal decomposition of metal-oleate complex. For 6 nm FeNP, 3 10^{-1} mol of iron oxide hydroxide. 12 ml of oleic acid and 10 ml of octadecene were added to a 50 ml three-neck round flask. Afterwards, the flask was stirred at 180 °C under Ar atmosphere and without condenser for 60 minutes to promote the evaporation of water and volatiles and the formation of a homogeneous light-brown solution of iron oleate. Afterward, the round flask was connected to a condenser and the suspension was heated to 320 °C with a heating ramp of 5 °C min^{-1}. After a few minutes, the solution turned dark brown, indicating the formation of iron nanoparticles.

The reaction time was settled in 60 min, followed by cooling down naturally at room temperature. In a final step, the colloidal nanoparticles were recovered from the organic suspension by adding 25 ml of a hexane/ethanol mixture 30 : 70% v/v. and the product could be easily recovered by centrifugation at 9000 rpm for 10 min. The procedure was repeated 3 times. The final product was easily dispersed and stored in hexane, forming a stable suspension of 15 mg Fe ml^{-1}.

4.2 Catalyst preparation

The catalysts were prepared by wet impregnation. In a typical protocol, 200 mg of the support was impregnated with 750 μl of the FeNPs suspension and an additional 750 μl of hexane. The nominal metal loading was fixed at 5% wt. The catalysts were sonicated for 15 minutes to promote the dispersion of the colloids onto the support and then dried overnight at room temperature.

4.3 Catalytic CH_4 decomposition

The catalytic tests combined with *in situ* XRD measurements were performed using a PAN-Analytical X'PERT PRO diffractometer equipped with an Anton Paar XRK-900 furnace, using Ni filtered Cu Kα radiation. The furnace was connected to a gas handling system able to provide He, N_2, H_2 and CH_4 controlled by their respective mass flow controllers.

The catalytic experiments were carried out at atmospheric pressure and 750 °C. 50 mg of the powder sample was loaded and heated to 300 °C with a heating rate of 5 K min^{-1} under vacuum for 2 h. Afterwards, the catalysts were activated under 100 ml min^{-1} flow of 50% H2/He. After 5 minutes, hydrogen was switched off and 50 ml min^{-1} CH_4 was fed, leading to 50% CH_4 in He. The reaction was kept for 90 minutes. XRD diffractograms were collected from 20° to 55° and a scan rate of 1.3° min^{-1} at different temperature steps and at room temperature before and after each experiment.

4.4 Characterization

The morphology and size distribution of the nanoparticles were analyzed by Transmission Electron Microscopy (TEM) in a FEI Tecnai T20 microscope operating at 200 kV, using a FEI single tilt holder. Samples were prepared by direct contact with the powder catalysts on Lacey carbon 400-mesh gold grids (Agar scientific). The STEM-EDX experiments and associated HAADF images were performed in a thermofisher Spectra Ultra microscope operated at 300 kV with a convergence angle of 24 mrad, a HAADF collection angle of 73–200 mrad and a camera length of 100 mm. EDX maps were acquired using an ultra-X detector for approx. 15 minutes per map.

In situ TEM experiments were performed in a FEI Titan ETEM operating a 300 kV. A differential pumping system is employed for the dosing of reacting gases into the microscope column. For the sample preparation, a few milligrams of the $MgAl_2O_4$ support are dispersed in 2 ml of absolute ethanol and homogenized to have a stable suspension. One microliter of the suspension is drop-casted on the center of the wildfire® microchip (Denssolutions, previously cleaned with plasma) and left to room temperature for drying. Afterwards, one microliter of 1 : 1000 dilution of FeNP was drop-cast and left drying at room temperature. Employing this strategy, it is possible to image not only supported FeNPs but also free-standing nanoparticles in the edges of the silicon windows of the chip.

For the experiment, the sample was heated to 700 °C under 1 mbar H_2 employing a heating rate of 11 °C min^{-1} and kept for 3 h. Afterwards, CH_4 was fed reaching a total pressure in the column of approximately 2 mbar. For the beam-enhanced experiment, the electron beam was focused over the specimen leading to an electron dose of $3 \cdot 10^3$ e^- $Å^{-2}$ s^{-1}. The micrographs were acquired with an acquisition of 2 frames per second.

Scanning electron microscopy studies (SEM) were performed on a Helios 5 Hydra Dual Beam (ThermoFisher Scientific) operating a 5 kV and 0.2 nA. Samples were prepared by direct contact with the powder catalysts on Lacey carbon 400-mesh gold grids (Agar scientific).

Raman spectra were recorded using the 647 nm emission of a Krypton ion laser (Innova 300c, Coherent) for excitation and a confocal Raman spectrometer (Lab Ram HR-800 Jobin Yvon) equipped with a liquid-nitrogen cooled charge-coupled device (CCD) camera for data acquisition. The typical laser power at the sample was 1 mW. Spectra were acquired for 5 × 10 s.

XPS data were collected using the Theta Probe X-ray Photoelectron Spectrometer from Thermo Scientific™ with a monochromatic Al Kα X-ray source (1486.68 eV). The XPS spot size was set to 400 μm, the pass energy to 50 eV, and the step size to 0.1 eV. For each core level, 50 scans were averaged. The data analysis and peak fitting was performed using Avantage software.

Data availability

Data for this article are available at Zenodo (EU Open Research Repository) at **https://doi.org/10.5281/zenodo.15296532**.

Author contributions

Esteban Gioria: investigation, methodology, formal analysis, writing – original draft, conceptualization. Filippo Romeggio: investigation, writing – original draft. Ruben Bueno Villoro: investigation. Ilenia Giarnieri: investigation. Patricia Benito: review, Ib Chorkendorff: review. Christian D. Damsgaard: review, resources, supervision.

Conflicts of interest

There are no conflicts to declare.

Acknowledgements

This work was supported by the European Research Council (ERC) STORMING project under the European Union's Horizon 2020 research and innovation program (grant agreement no. 101069690), the Danish National Research Foundation (DNRF146) and by the MSCA-Innovative Training Network Catchy (grant agreement no. 955650).

References

1 E. Gioria, S. Li, A. Mazheika, R. Naumann d'Alnoncourt, A. Thomas and F. Rosowski, CuNi Nanoalloys with Tunable Composition and Oxygen Defects for the Enhancement of the Oxygen Evolution Reaction, *Angew. Chem., Int. Ed.*, 2023, **62**(26), e202217888, DOI: **10.1002/anie.202217888**.

2 T. W. Deelen, C. Hernández Mejía and K. P. Jong, Control of metal–support interactions in heterogeneous catalysts to enhance activity and selectivity, *Nat. Catal.*, 2019, **2**(11), 955–970, DOI: **10.1038/s41929-019-0364-x**.

3 E. Gioria, R. Naumann d'Alnoncourt, A. Thomas and F. Rosowski, Size, Shape and Composition Control of Metallic Colloidal Nanoparticles for the Design of Heterogeneous Catalysts, *ChemCatChem*, 2025, **17**(11), e202401701, DOI: **10.1002/cctc.202401701**.

4 E. Gioria, F. Marchesini, A. Soldati, A. Giorello, J. Hueso and L. Gutierrez, Green Synthesis of a Cu/SiO_2 Catalyst for Efficient H2-SCR of NO, *Appl. Sci.*, 2019, **9**(19), 4075–4092, DOI: **10.3390/app9194075**.

5 S. Zhang, P. N. Plessow, J. J. Willis, S. Dai, M. Xu, G. W. Graham, M. Cargnello, F. Abild-Pedersen and X. Pan, Dynamical Observation and Detailed Description of Catalysts under Strong Metal–Support Interaction, *Nano Lett.*, 2016, **16**(7), 4528–4534, DOI: **10.1021/acs.nanolett.6b01769**.

6 E. Gioria, P. Ingale, F. Pohl, R. Naumann d'Alnoncourt, A. Thomas and F. Rosowski, Boosting the performance of Ni/Al_2O_3 for the reverse water gas shift reaction through formation of CuNi nanoalloys, *Catal. Sci. Technol.*, 2022, **12**(2), 474–487, DOI: **10.1039/D1CY01585K**.

7 J. Santos, Metal–support interactions between iron and titania for catalysts prepared by thermal decomposition of iron pentacarbonyl and by impregnation, *J. Catal.*, 1983, **81**(1), 147–167, DOI: **10.1016/0021-9517(83)90154-9**.

8 R. Spretz, S. G. Marchetti, M. A. Ulla and E. A. Lombardo, Fe/MgO Formulations for the Catalytic Combustion of Methane, *J. Catal.*, 2000, **194**(2), 167–174, DOI: **10.1006/jcat.2000.2921**.

9 M. Cargnello, Colloidal Nanocrystals as Building Blocks for Well-Defined Heterogeneous Catalysts, *Chem. Mater.*, 2019, **31**(3), 576–596, DOI: **10.1021/acs.chemmater.8b04533**.

10 K. J. Hughes, K. A. Iyer, R. E. Bird, J. Ivanov, S. Banerjee, G. Georges and Q. A. Zhou, Review of Carbon Nanotube Research and Development: Materials and Emerging Applications, *ACS Appl. Nano Mater.*, 2024, **7**(16), 18695–18713, DOI: **10.1021/acsanm.4c02721**.

11 J. Wang, H. Jia, Z. Liu, J. Yu, L. Cheng, H. Wang, F. Cui and G. Zhu, Anchoring π-d Conjugated Metal–Organic Frameworks with Dual-Active Centers on Carbon Nanotubes for Advanced Potassium-Ion Batteries, *Adv. Mater.*, 2024, **36**(6), 2305605, DOI: **10.1002/adma.202305605**.

12 J.-Z. Yen, C.-B. Chang, K.-S. Jhang and H.-Y. Tuan, Excellent Metal Phosphide Electrode for Potassium Ion Hybrid Capacitors: The Case of Carbon Nanotube-Wrapped AgP_2, *ACS Appl. Energy Mater.*, 2023, **6**(2), 822–831, DOI: **10.1021/acsaem.2c03113**.

13 S. Rasouli, D. Myers, K. Higashida, N. Nakashima, P. Crozier and P. Ferreira, Electrochemical Evolution of Fuel Cell Platinum Nanocatalysts on Carbon Nanotubes at the Atomic Scale, *ACS Appl. Energy Mater.*, 2023, **6**(23), 11861–11873, DOI: **10.1021/acsaem.3c01765**.

14 B. J. Leal Pérez, J. A. Medrano Jiménez, R. Bhardwaj, E. Goetheer, M. Sint Annaland and F. Gallucci, Methane pyrolysis in a molten gallium bubble column reactor for sustainable hydrogen production: proof of concept & techno-economic assessment, *Int. J. Hydrogen Energy*, 2021, **46**(7), 4917–4935, DOI: **10.1016/j.ijhydene.2020.11.079**.

15 P. C. K. Vesborg and T. F. Jaramillo, Addressing the terawatt challenge: scalability in the supply of chemical elements for renewable energy, *RSC Adv.*, 2012, **2**(21), 7933, DOI: **10.1039/c2ra20839c**.

16 N. Sánchez-Bastardo, R. Schlögl and H. Ruland, Methane Pyrolysis for Zero-Emission Hydrogen Production: A Potential Bridge Technology from Fossil Fuels to a Renewable and Sustainable Hydrogen Economy, *Ind. Eng. Chem. Res.*, 2021, **60**(32), 11855–11881, DOI: **10.1021/ACS.IECR.1C01679**.

17 Y. Li, W. Kim, Y. Zhang, M. Rolandi, D. Wang and H. Dai, Growth of Single-Walled Carbon Nanotubes from Discrete Catalytic Nanoparticles of Various Sizes, *J. Phys. Chem. B*, 2001, **105**(46), 11424–11431, DOI: **10.1021/jp012085b**.

18 Y. Li, J. Liu, Y. Wang and Z. L. Wang, Preparation of Monodispersed FeMo Nanoparticles as the Catalyst for CVD Synthesis of Carbon Nanotubes, *Chem. Mater.*, 2001, **13**(3), 1008–1014, DOI: **10.1021/cm000787s**.

19 H. Ago, K. Nakamura, N. Uehara and M. Tsuji, Roles of MetalSupport Interaction in Growth of Single- and Double-Walled Carbon Nanotubes Studied with Diameter-Controlled Iron Particles Supported on MgO, *J. Phys. Chem. B*, 2004, **108**(49), 18908–18915, DOI: **10.1021/jp046856y**.

20 H. Ago, K. Nakamura, S. Imamura and M. Tsuji, Growth of double-wall carbon nanotubes with diameter-controlled iron oxide nanoparticles supported on MgO, *Chem. Phys. Lett.*, 2004, **391**(4–6), 308–313, DOI: 10.1016/j.cplett.2004.04.110.

21 N. Arora, S. Amsarajan and B. R. Jagirdar, Morphological Evolution in Air-Stable Metallic Iron Nanostructures and Their Magnetic Study, *J. Phys. Chem. C*, 2015, **119**(1), 665–674, DOI: 10.1021/jp508706k.

22 O. Mykhailiv, H. Zubyk and M. E. Plonska-Brzezinska, Carbon nano-onions: unique carbon nanostructures with fascinating properties and their potential applications, *Inorg. Chim. Acta*, 2017, **468**, 49–66, DOI: 10.1016/j.ica.2017.07.021.

23 S. J. Han, S. W. Lee, H. W. Kim, S. K. Kim and Y. T. Kim, Nonoxidative Direct Conversion of Methane on Silica-Based Iron Catalysts: Effect of Catalytic Surface, *ACS Catal.*, 2019, **9**(9), 7984–7997, DOI: 10.1021/acscatal.9b01643.

24 L. Zhou, L. R. Enakonda, S. Li, D. Gary, P. Del-Gallo, C. Mennemann and J. M. Basset, Iron ore catalysts for methane decomposition to make CO*x* free hydrogen and carbon nano material, *J. Taiwan Inst. Chem. Eng.*, 2018, **87**, 54–63, DOI: 10.1016/j.jtice.2018.03.008.

25 C. T. Wirth, B. C. Bayer, A. D. Gamalski, S. Esconjauregui, R. S. Weatherup, C. Ducati, C. Baehtz, J. Robertson and S. Hofmann, The Phase of Iron Catalyst Nanoparticles during Carbon Nanotube Growth, *Chem. Mater.*, 2012, **24**(24), 4633–4640, DOI: 10.1021/cm301402g.

26 S. Pathak and E. McFarland, Iron Catalyzed Methane Pyrolysis in a Stratified Fluidized Bed Reactor, *Energy Fuels*, 2024, **38**(14), 12576–12585, DOI: 10.1021/acs.energyfuels.4c01484.

27 D. Wilson and M. A. Langell, XPS analysis of oleylamine/oleic acid capped Fe_3O_4 nanoparticles as a function of temperature, *Appl. Surf. Sci.*, 2014, **303**, 6–13, DOI: 10.1016/j.apsusc.2014.02.006.

28 P. Cheah, T. Cowan, R. Zhang, A. Fatemi-Ardekani, Y. Liu, J. Zheng, F. Han, Y. Li, D. Cao and Y. Zhao, Continuous growth phenomenon for direct synthesis of monodisperse water-soluble iron oxide nanoparticles with extraordinarily high relaxivity, *Nanoscale*, 2020, **12**(16), 9272–9283, DOI: 10.1039/D0NR01552K.

29 X. Chen, X. Wang and D. Fang, A review on C1s XPS-spectra for some kinds of carbon materials. Fullerenes, Nanotubes and Carbon Nanostructures, *Fullerenes, Nanotubes Carbon Nanostruct.*, 2020, **28**(12), 1048–1058, DOI: 10.1080/1536383X.2020.1794851.

30 Z. Qu, C. Wan and W. Pan, Thermal Expansion and Defect Chemistry of MgO-Doped $Sm_2Zr_2O_7$, *Chem. Mater.*, 2007, **19**(20), 4913–4918, DOI: 10.1021/cm071615z.

31 P. B. Amama, C. L. Pint, F. Mirri, M. Pasquali, R. H. Hauge and B. Maruyama, Catalyst–support interactions and their influence in water-assisted carbon nanotube carpet growth, *Carbon*, 2012, **50**(7), 2396–2406, DOI: 10.1016/j.carbon.2012.01.045.

32 G. Bond, K. Molloy and F. Stone, Reduction of MgO-supported iron oxide: formation and characterization of Fe/MgO catalysts, *Solid State Ionics*, 1997, **101–103**(103), 697–705, DOI: 10.1016/S0167-2738(97)00179-3.

33 H. Mousty, E. G. Derouane, B. S. Clausen and H. Topsøe, Role of The Metal–Support Interaction in the Preparation of Fe/MgO Catalysts, *Stud. Surf. Sci. Catal.*, 1983, **16**, 385–394, DOI: 10.1016/S0167-2991(09)60035-5. https://linkinghub.elsevier.com/retrieve/pii/S0167299109600355.

34 M. Niedermaier, T. Schwab, P. Dolcet, J. Bernardi, S. Gross, M. Bockstedte and O. Diwald, Cobalt and Iron Ions in MgO Nanocrystals: Should They Stay or Should They Go, *J. Phys. Chem. C*, 2019, **123**(42), 25991–26004, DOI: 10.1021/acs.jpcc.9b07350.

35 G. BOND, Reduction of MgO-supported iron oxide: formation and characterization of Fe/MgO catalysts, *Solid State Ionics*, 1997, **101–103**(103), 697–705, DOI: 10.1016/S0167-2738(97)00179-3.

36 L. Di Felice, C. Courson, D. Niznansky, P. U. Foscolo and A. Kiennemann, Biomass Gasification with Catalytic Tar Reforming: A Model Study into Activity Enhancement of Calcium- and Magnesium-Oxide-Based Catalytic Materials by Incorporation of Iron, *Energy Fuels*, 2010, **24**(7), 4034–4045, DOI: 10.1021/ef100351j.

37 H. Kathyayini, N. Nagaraju, A. Fonseca and J. B. Nagy, Catalytic activity of Fe, Co and Fe/Co supported on Ca and Mg oxides, hydroxides and carbonates in the synthesis of carbon nanotubes, *J. Mol. Catal. A: Chem.*, 2004, **223**(1–2), 129–136, DOI: 10.1016/j.molcata.2004.02.029.

38 J. Yu, T. Zhang, H. Xu, X. Dong, Y. Cai, Y. Pan and C. Cao, Thermostable iron oxide nanoparticle synthesis within recombinant ferritins from the hyperthermophile *Pyrococcus yayanosii* CH1, *RSC Adv.*, 2019, **9**(67), 39381–39393, DOI: 10.1039/C9RA07397C.

39 J. R. Shallenberger, D. A. Cole and S. W. Novak, Characterization of silicon oxynitride thin films by X-ray photoelectron spectroscopy, *J. Vac. Sci. Technol., A*, 1999, **17**(4), 1086–1090, DOI: 10.1116/1.582038.

40 F. Li, X. Yue, Y. Liao, L. Qiao, K. Lv and Q. Xiang, Understanding the unique S-scheme charge migration in triazine/heptazine crystalline carbon nitride homojunction, *Nat. Commun.*, 2023, **14**(1), 3901, DOI: 10.1038/s41467-023-39578-z.

41 L. C. Chen, C. Y. Yang, D. M. Bhusari, K. H. Chen, M. C. Lin, J. C. Lin and T. J. Chuang, Formation of crystalline silicon carbon nitride films by microwave plasma-enhanced chemical vapor deposition, *Diamond Relat. Mater.*, 1996, **5**(3–5), 514–518, DOI: 10.1016/0925-9635(96)80070-7.

42 I. AlShibane, J. S. J. Hargreaves, A. L. Hector, W. Levason and A. McFarlane, Synthesis and methane cracking activity of a silicon nitride supported vanadium nitride nanoparticle composite, *Dalton Trans.*, 2017, **46**(27), 8782–8787, DOI: 10.1039/C7DT00285H.

43 D. Hullmann, G. Wendt, U. Šingliar and G. Ziegenbalg, Propane dehydrogenation over supported platinum silicon nitride catalysts, *Appl. Catal., A*, 2002, **225**(1–2), 261–270, DOI: 10.1016/S0926-860X(01)00871-7.

44 F. J. Cadete Santos Aires and J. C. Bertolini, On the Use of Silicon Nitride in Catalysis, *Top. Catal.*, 2009, **52**(11), 1492–1505, DOI: 10.1007/s11244-009-9296-z.

45 J. C. DeMuth, Y. L. Kim, J. N. Hall, Z. H. Syed, K. Deng, F. A. Perras, M. S. Ferrandon, A. J. Kropf, C. Liu, D. M. Kaphan and M. Delferro, Silicon Nitride Surface Enabled Propane Dehydrogenation Catalyzed by Supported Organozirconium, *J. Am. Chem. Soc.*, 2024, **146**(21), 14404–14409, DOI: 10.1021/jacs.4c02776.

46 W. Z. Li, L. Kovarik, D. Mei, J. Liu, Y. Wang and C. H. F. Peden, Stable platinum nanoparticles on specific $MgAl_2O_4$ spinel facets at high temperatures in oxidizing atmospheres, *Nat. Commun.*, 2013, **4**, 2481, DOI: 10.1038/ncomms3481.

47 D. H. Kim, J.-R. Youn, J.-C. Seo, S. B. Kim, M.-J. Kim and K. Lee, One-pot synthesis of NiCo/$MgAl_2O_4$ catalyst for high coke-resistance in steam methane reforming: Optimization of Ni/Co ratio, *Catal. Today*, 2023, **411–412**, 113910, DOI: 10.1016/j.cattod.2022.09.016.

48 I. Giarnieri, A. D. Bobitan, V. Foderà, E. Gioria, L. Costley-Wood, A. Bertuzzi, F. Ospitali, G. Fornasari, C. D. Damsgaard, S. D. M. Jacques, M. C. Righi, P. Benito and A. M. Beale, *Methane Splitting to Hydrogen and Base Growth Carbon Nanotubes Over Fe-Based Catalysts*, 2025, DOI: 10.2139/ssrn.5184590. https://www.ssrn.com/abstract=5184590.

49 M. Pudukudy, Z. Yaakob and M. S. Takriff, Methane decomposition over Pd promoted Ni/$MgAl_2O_4$ catalysts for the production of CO*x* free hydrogen and multiwalled carbon nanotubes, *Appl. Surf. Sci.*, 2015, **356**, 1320–1326, DOI: 10.1016/j.apsusc.2015.08.246.

50 A. Ota, E. L. Kunkes, J. Kröhnert, M. Schmal and M. Behrens, Particle size effect in methane activation over supported palladium nanoparticles, *Appl. Catal., A*, 2013, **452**, 203–213, DOI: 10.1016/j.apcata.2012.11.021.

51 G. D. B. Nuernberg, E. L. Foletto, C. E. M. Campos, H. V. Fajardo, N. L. V. Carreño and L. F. D. Probst, Direct decomposition of methane over Ni catalyst supported in magnesium aluminate, *J. Power Sources*, 2012, **208**, 409–414, DOI: 10.1016/j.jpowsour.2012.02.037.

52 G. D. B. Nuernberg, H. V. Fajardo, E. L. Foletto, S. M. Hickel-Probst, N. L. V. Carreño, L. F. D. Probst and J. Barrault, Methane conversion to hydrogen and nanotubes on Pt/Ni catalysts supported over spinel $MgAl_2O_4$, *Catal. Today*, 2011, **176**(1), 465–469, DOI: 10.1016/j.cattod.2010.10.053.

53 G. B. Nuernberg, E. L. Foletto, L. F. D. Probst, N. L. V. Carreño and M. A. Moreira, $MgAl_2O_4$ spinel particles prepared by metal–chitosan complexation route and used as catalyst support for direct decomposition of methane, *J. Mol. Catal. A: Chem.*, 2013, **370**, 22–27, DOI: 10.1016/j.molcata.2012.12.007.

54 C. García-Sancho, R. Guil-López, A. Sebastián-López, R. M. Navarro and J. L. G. Fierro, Hydrogen production by methane decomposition: a comparative study of supported and bulk ex-hydrotalcite mixed oxide catalysts with Ni, Mg and Al, *Int. J. Hydrogen Energy*, 2018, **43**(20), 9607–9621, DOI: 10.1016/j.ijhydene.2018.04.021.

55 Z. Haijun, J. Xiaolin, L. Zhanjie and L. Zhenzhen, The low temperature preparation of nanocrystalline $MgAl_2O_4$ spinel by citrate sol–gel process, *Mater. Lett.*, 2004, **58**(10), 1625–1628, DOI: 10.1016/j.matlet.2003.09.051.

56 S. A. Chernyak, A. S. Ivanov, D. N. Stolbov, T. B. Egorova, K. I. Maslakov, Z. Shen, V. V. Lunin and S. V. Savilov, N-doping and oxidation of carbon nanotubes and jellyfish-like graphene nanoflakes through the prism of Raman spectroscopy, *Appl. Surf. Sci.*, 2019, **488**, 51–60, DOI: 10.1016/j.apsusc.2019.05.243.

57 R. A. DiLeo, B. J. Landi and R. P. Raffaelle, Purity assessment of multiwalled carbon nanotubes by Raman spectroscopy, *J. Appl. Phys.*, 2007, **101**(6), 064307, DOI: 10.1063/1.2712152.

58 C. C. Zhang, S. Hartlaub, I. Petrovic and B. Yilmaz, Raman Spectroscopy Characterization of Amorphous Coke Generated in Industrial Processes, *ACS Omega*, 2022, **7**(3), 2565–2570, DOI: 10.1021/acsomega.1c03456.

59 A. Coccato, J. Jehlicka, L. Moens and P. Vandenabeele, Raman spectroscopy for the investigation of carbon-based black pigments, *J. Raman Spectrosc.*, 2015, **46**(10), 1003–1015, DOI: 10.1002/jrs.4715.

60 H. Yoshida, S. Takeda, T. Uchiyama, H. Kohno and Y. Homma, Atomic-Scale *In situ* Observation of Carbon Nanotube Growth from Solid State Iron Carbide Nanoparticles, *Nano Lett.*, 2008, **8**(7), 2082–2086, DOI: 10.1021/nl080452q.

61 M. He, B. Liu, A. I. Chernov, E. D. Obraztsova, I. Kauppi, H. Jiang, I. Anoshkin, F. Cavalca, T. W. Hansen, J. B. Wagner, A. G. Nasibulin, E. I. Kauppinen, J. Linnekoski, M. Niemelä and J. Lehtonen, Growth Mechanism of Single-Walled Carbon Nanotubes on Iron–Copper Catalyst and Chirality Studies by Electron Diffraction, *Chem. Mater.*, 2012, **24**(10), 1796–1801, DOI: 10.1021/cm300308k.

62 X. Liu, C. Zhang, Y. Li, J. W. Niemantsverdriet, J. B. Wagner and T. W. Hansen, Environmental Transmission Electron Microscopy (ETEM) Studies of Single Iron Nanoparticle Carburization in Synthesis Gas, *ACS Catal.*, 2017, **7**(7), 4867–4875, DOI: 10.1021/ACSCATAL.7B00946/ASSET/IMAGES/LARGE/CS-2017-00946J_0008.

63 X. Feng, S. W. Chee, R. Sharma, K. Liu, X. Xie, Q. Li, S. Fan and K. Jiang, *In Situ* TEM observation of the gasification and growth of carbon nanotubes using iron catalysts, *Nano Res.*, 2011, **4**(8), 767–779, DOI: 10.1007/s12274-011-0133-x.

64 X. Huang, R. Farra, R. Schlögl and M.-G. Willinger, Growth and Termination Dynamics of Multiwalled Carbon Nanotubes at Near Ambient Pressure: An *In Situ* Transmission Electron Microscopy Study, *Nano Lett.*, 2019, **19**(8), 5380–5387, DOI: 10.1021/acs.nanolett.9b01888.

65 L. Zhang, D. Tang and C. Liu, Growth Mechanism of Carbon Nanotubes Revealed by *In Situ* Transmission Electron Microscopy, *Small*, 2024, **20**(50), 2405736, DOI: 10.1002/smll.202405736.

66 L. ReddyEnakonda, L. Zhou, Y. Saih, S. Ould-Chikh, S. Lopatin, D. Gary, P. Del-Gallo and J. Basset, Methane-induced Activation Mechanism of Fused Ferric Oxide–Alumina Catalysts during Methane Decomposition,

ChemSusChem, 2016, **9**(15), 1911–1915, DOI: **10.1002/cssc.201600500**.

67 K. Song, D. J. Sauter, J. Wu, V. P. Dravid and P. C. Stair, Evolution of High-Energy Electron Beam Irradiation Effects on Zeolite Supported Catalyst: Metal Nanoprecipitation, *ACS Catal.*, 2012, **2**(3), 384–390, DOI: **10.1021/cs300002c**.

68 A. Ziashahabi, A. Elsukova, S. Nilsson, M. Beleggia, P. Stanley Jørgensen, C. Langhammer and S. Kadkhodazadeh, Electron Beam Induced Enhancement and Suppression of Oxidation in Cu Nanoparticles in Environmental Scanning Transmission Electron Microscopy, *ACS Nanosci. Au*, 2023, 389–397, DOI: **10.1021/acsnanoscienceau.3C00018**.

69 C. M. Wang, D. R. Baer, J. E. Amonette, M. H. Engelhard, J. J. Antony and Y. Qiang, Electron beam-induced thickening of the protective oxide layer around Fe nanoparticles, *Ultramicroscopy*, 2007, **108**(1), 43–51, DOI: **10.1016/j.ultramic.2007.03.002**.

70 S. Raabe, D. Mierwaldt, J. Ciston, M. Uijttewaal, H. Stein, J. Hoffmann, Y. Zhu, P. Blöchl and C. Jooss, In Situ Electrochemical Electron Microscopy Study of Oxygen Evolution Activity of Doped Manganite Perovskites, *Adv. Funct. Mater.*, 2012, **22**(16), 3378–3388, DOI: **10.1002/adfm.201103173**.

71 J. A. Sundararajan, M. Kaur and Y. Qiang, Mechanism of Electron Beam Induced Oxide Layer Thickening on Iron–Iron Oxide Core–Shell Nanoparticles, *J. Phys. Chem. C*, 2015, **119**(15), 8357–8363, DOI: **10.1021/acs.jpcc.5b00943**.

72 M. Lin, J. P. Y. Tan, C. Boothroyd, K. P. Loh, E. S. Tok and Y. L. Foo, Dynamical observation of bamboo-like carbon nanotube growth, *Nano Lett.*, 2007, **7**(8), 2234–2238, DOI: **10.1021/nl070681x**.

73 J.-Y. Yoon, J. Park, K. Lee, O. F. Jafter, M. Jang, J. Cheon, K. Kim and D. Lungerich, Understanding Electron Beam-Induced Chemical Polymerization Processes of Small Organic Molecules Using Operando Liquid-Phase Transmission Electron Microscopy, *ACS Nano*, 2025, **19**(11), 10889–10901, DOI: **10.1021/acsnano.4c15470**.

74 E. Gioria, V. K. Ocampo-Restrepo, A. S. Bjørnlund, V. K. Pedersen, S. Helveg, I. Chorkendorff and C. D. Damsgaard, CH_4 Decomposition on Nickel Phyllosilicate: Switching from Tip to Base Growth of Carbon Nanotubes, *Small*, 2025, 2500994, DOI: **10.1002/smll.202500994**.

75 X. Yao, Y. Wei, Z. Wang and L. Gan, Revealing the Role of Surface Composition on the Particle Mobility and Coalescence of Carbon-Supported Pt Alloy Fuel Cell Catalysts by *In Situ* Heating (S)TEM, *ACS Catal.*, 2020, **10**(13), 7381–7388, DOI: **10.1021/acscatal.0c01765**.

76 X. Chen, C. Li, B. Li, Y. Ying, S. Ye, D. N. Zakharov, S. Hwang, J. Fang, G. Wang, Y.-J. Hu and G. Zhou, Surface Self-Diffusion Induced Sintering of Nanoparticles, *ACS Nano*, 2024, **18**(45), 31160–31173, DOI: **10.1021/acsnano.4c09056**.

77 T. W. Hansen, A. T. Delariva, S. R. Challa and A. K. Datye, Sintering of catalytic nanoparticles: particle migration or ostwald ripening?, *Acc. Chem. Res.*, 2013, **46**(8), 1720–1730, DOI: **10.1021/ar3002427**.

78 M. Guo, Q. Meng, M. Gao, L. Zheng, Q. Li, L. Jiao and H. Jiang, Single-Atom Pt Loaded on MOF-Derived Porous TiO_2 with Maxim-Ized Pt Atom Utilization for Selective Hydrogenation of Halonitro-benzene, *Angew. Chem., Int. Ed.*, 2025, **64**(7), e202418964, DOI: **10.1002/anie.202418964**.

79 A. M. Roth-Zawadzki, A. J. Nielsen, R. E. Tankard and J. Kibsgaard, Dual and Triple Atom Electrocatalysts for Energy Conversion (CO_2RR, NRR, ORR, OER, and HER): Synthesis, Characterization, and Activity Evaluation, *ACS Catal.*, 2024, **14**(2), 1121–1145, DOI: **10.1021/acscatal.3c05000**.

80 J. Xian, S. Li, H. Su, P. Liao, S. Wang, Y. Zhang, W. Yang, J. Yang, Y. Sun, Y. Jia, Q. Liu, Q. Liu and G. Li, Electrocatalytic Synthesis of Essential Amino Acids from Nitric Oxide Using Atomically Dispersed Fe on N-doped Carbon, *Angew. Chem., Int. Ed.*, 2023, **62**(26), e202304007, DOI: **10.1002/anie.202304007**.

81 X. Zhao, P. Pachfule and A. Thomas, Covalent organic frameworks (COFs) for electrochemical applications, *Chem. Soc. Rev.*, 2021, **50**(12), 6871–6913, DOI: **10.1039/D0CS01569E**.

82 Z. Mao and C. T. Campbell, Predicting a Key Catalyst-Performance Descriptor for Supported Metal Nanoparticles: Metal Chemical Potential, *ACS Catal.*, 2021, **11**(13), 8284–8291, DOI: **10.1021/acscatal.1c01870**.

83 S. L. Hemmingson and C. T. Campbell, Trends in Adhesion Energies of Metal Nanoparticles on Oxide Surfaces: Understanding Support Effects in Catalysis and Nanotechnology, *ACS Nano*, 2017, **11**(2), 1196–1203, DOI: **10.1021/acsnano.6b07502**.

84 M. L. Weber, D. Jennings, S. Fearn, A. Cavallaro, M. Prochazka, A. Gutsche, L. Heymann, J. Guo, L. Yasin, S. J. Cooper, J. Mayer, W. Rheinheimer, R. Dittmann, R. Waser, O. Guillon, C. Lenser, S. J. Skinner, A. Aguadero, S. Nemšák and F. Gunkel, Thermal stability and coalescence dynamics of exsolved metal nanoparticles at charged perovskite surfaces, *Nat. Commun.*, 2024, **15**(1), 9724, DOI: **10.1038/s41467-024-54008-4**.

85 D. Leybo, U. J. Etim, M. Monai, S. R. Bare, Z. Zhong and C. Vogt, Metal–support interactions in metal oxide-supported atomic, *Cluster, and Nanoparticle Catalysis*. Royal Society of Chemistry, 2024, DOI: **10.1039/d4cs00527a**.